# Design and Quantitative Analysis of Asymmetric Flux Reversal Permanent Magnet Linear Machine with Reduced Leakage Flux

Yiming Shen[1], Zhaokai Li[2], Zhuo Chen[3]

[1]School of Electrical and Electronic Engineering, Nanyang Technological University, Singapore
[2]Department of Energy, Politecnico di Milano, Milano MI 20156, Italy
[3]College of Electrical Engineering, Zhejiang University, Hangzhou 310027, China

**This paper introduces an asymmetric flux reversal permanent magnet linear machine (AFR-PMLM) designed to minimize leakage flux. By employing asymmetric Halbach PM array, it effectively generates and fully exploits the second-order harmonic magnetomotive force (MMF), leading to substantial improvements in both thrust force density and power factor compared to conventional FR-PMLM. Firstly, the machine topology and operation principle are introduced. Subsequently, the thrust force generation mechanism under multi MMFs is analytically calculated based on MMF-permeance model. Furthermore, various electromagnetic performances are thoroughly illustrated and comprehensively studied. It reveals that the proposed AFR-PMLM with Halbach PM array has the capability to provide 12.8% and 55.4% higher average force than that in AFR-PMLM with conventional asymmetric PM excitation and conventional FR-PMLM, respectively. Additionally, it achieves a power factor exceeding 0.77 under a current density of 6 A/mm$^2$, representing a notable improvement of 36.8% compared to conventional FR-PMLM with symmetric PM excitation. Compared with conventional PMLM, it can provide nearly 72.1% of the thrust force density while consuming only 1/81 of the PMs over a 10-meter distance.**

***Index Terms*—Asymmetric excitation, flux reversal, linear machine, permanent magnet, primary excitation.**

## I. Introduction

PERMANENT magnet linear machines (PMLMs) have the unique capability of directly conveying linear motion without the need for intermediary transmissions, making them highly versatile across various fields including transportation, industrial servo systems, wave energy generation and piston engine generators [1]-[3]. PMLMs boast exceptional features such as high force density, high precision, high dynamic response, and high reliability. However, achieving such high performance always entails significant costs, particularly with the utilization of rare-earth PMs. Consequently, there is a growing emphasis in both academia and industry on developing techniques to enhance the thrust force density of PMLMs while minimizing the reliance on rare-earth PMs, addressing a pivotal area of research.

In conventional PMLMs designs, the long stator typically houses PMs, while the short mover consists of an armature winding. Some researchers have proposed consequent pole (CP) structures to reduce the usage of PMs in the long stator [4], [5]. However, the usage of PMs remains high even with CP structures, and the overall costs cannot be significantly reduced especially for long distance applications ranging from tens to hundreds of meters. In recent years, a new series of PMLMs with primary excitation (PE-PMLMs) has emerged, attracting growing attention. Unlike conventional PMLMs, PE-PMLMs integrate both the armature winding and PMs in the short mover (primary), while the long stator is made of a low-cost iron core without PMs. This design allows for a significant reduction in the usage of PMs, resulting in a substantial reduction in the overall cost of the machine. Some types of PE-PMLMs will be discussed in detail as follows.

Switched flux PMLMs (SF-PMLMs) incorporate PMs between two segmented primary cores to concentrate magnetic flux. Various designs have been explored to enhance force density, including multi-teeth structures, hybrid excitation, and doubly-fed structures [6]-[8]. However, the segmented parts in SF-PMLMs will lead to reliability and assembly issues, further limiting their practical applications. Moreover, flux reversal PMLMs (FR-PMLMs) have gained significant attention due to their simpler structure. Researchers have explored innovative excitation methods to enhance the performance, such as hybrid excitation and flux-concentrated structures [9]-[12]. These advancements indicate that the thrust force density can be effectively improved while the issues of low power factor and high leakage flux still require further improvement.

In order to enhance the thrust force density as well as the power factor, this paper introduces an asymmetric flux reversal permanent magnet linear machine (AFR-PMLM) with reduced leakage flux. Through the utilization of asymmetric Halbach PM array, the AFR-PMLM can efficiently generate and fully exploit second-order harmonic magnetomotive force (MMF), resulting in a substantial improvement in both thrust force density and power factor compared with conventional FR-PMLM. The topology and working principle are introduced in Section II. Then, the thrust force generation mechanism under multi MMFs will be analytically calculated based on MMF-permeance model in Section III. Various electromagnetic performances, such as the open circuit characteristics, thrust force performances and power factor are comparatively studied by using finite element method (FEM) in Section IV. Finally, the prototype of AFR-PMLM is fabricated to validate the FEM predicted results.

## II. Machine Topology and Working Principle

Fig. 1 illustrates the topologies of three types of flux reversal permanent magnet linear machine (FR-PMLM). For the proposed asymmetric flux reversal structure, the PMs with unequal widths and opposite polarity are surface-mounted on the primary teeth. Compared with conventional asymmetric PM excitation in Fig. 1(b) and symmetric PM excitation in Fig. 1(c), the Halbach PM array employed in Fig. 1(a) can effectively reduce the leakage flux between two main PMs with unequal width. Additionally, double-layer concentrated windings are wound on the primary teeth. The secondary consists solely of a salient iron core to modulate the magnetomotive force (MMF)

generated by the primary. Fig. 2 illustrates the variation of flux linkage at different positions. At positions A and C, where the secondary tooth aligns with the primary tooth, peak flux linkage is achieved in the respective coils. Conversely, when the primary slot aligns with the secondary slot or tooth, the magnetic flux only links the secondary, resulting in minimal flux linkage in the coils. As a result, flux linkage in both coils follows a sinusoidal and bipolar waveform. Additionally, since two secondary PMs in Halbach PM array are magnetized in the opposite direction of the leakage flux loop, some of the leakage flux can be transferred into the main flux.

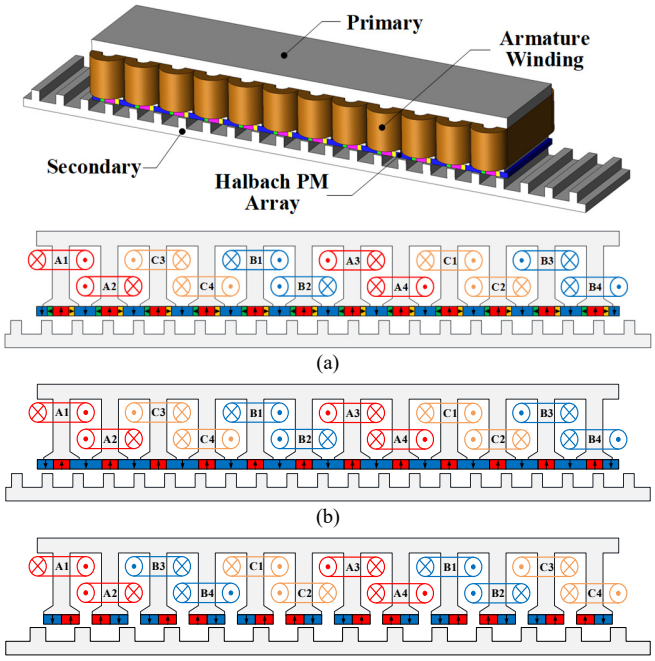


Fig. 1. Topologies of flux reversal PMLM. (a) The proposed AFR-PMLM with Halbach PM array. (b) AFR-PMLM with conventional asymmetric PM excitation. (c) Conventional FR-PMLM with symmetric PM excitation.

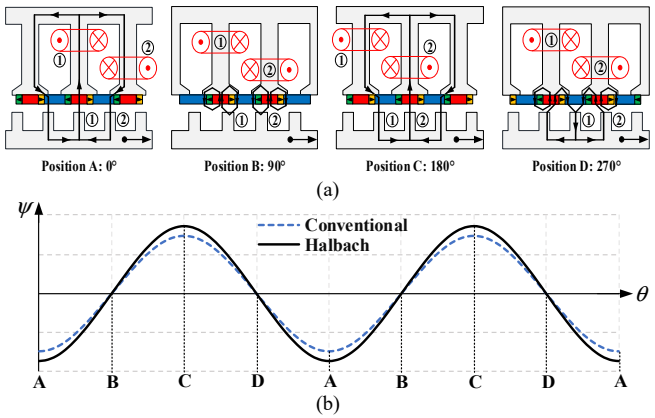


Fig. 2. Variation of flux linkage at different positions. (a) Schematic of simplified magnetic circuit. (b) Waveform of flux linkage.

To fully utilize the multiple magnetomotive forces (MMFs) resulting from asymmetric PM excitation, the number of secondary poles ($N_s$) will differ from that in conventional PMLMs with near slot and pole combination [13]. The optimal slot and pole combination can be expressed as:

$$\begin{cases} N_p = 2mj,\ j = 1,2,3\cdots \\ N_s = 3N_p/2 \pm k,\ k = 1,2\cdots \end{cases} \tag{1}$$

where $m$ is the phase number, $N_p$ is the number of primary slots, $N_s$ is the number of secondary poles. Then, the coil pitch factor ($k_p$), coil distribution factor ($k_d$) and winding factor ($k_w$) can be calculated as follows:

$$\begin{cases} k_p = \sin(\alpha/2), \alpha = \left(360N_s/N_p\right) \bmod 360 \\ k_d = \sin(b\theta_s/2)/\left(b\sin(\theta_s/2)\right) \\ k_w = k_p k_d \end{cases} \tag{2}$$

where $b$ is the least number of different EMF phasors for one phase, $\theta_s$ is the electrical degree between two EMF phasors.

Table I presents the feasible slot and pole combinations along with their corresponding winding factors ($k_w$) calculated using Eq. (1). For a given number of primary slots, two different secondary pole numbers that satisfy Eq. (1), namely ($3N_p/2 + k$) and ($3N_p/2$ - $k$), yield the same winding factor. When the number of secondary poles approaches $3N_p/2$, both the winding factor and thrust force density increase. However, it is also important to consider specific force requirements and machine dimensions. For instance, an excessive number of primary slots may lead to a compacted slot area, potentially reducing thrust force density. In this study, $N_p$ is chosen as 12, allowing $N_s$ to be set as 17 to achieve relatively high force density and low force ripple, denoted as 12s17p.

TABLE I
FEASIBLE SLOT/POLE COMBINATIONS AND WINDING FACTOR

| $N_p/N_s$ | 9/11 | 9/13 | 9/14 | 9/16 |
|---|---|---|---|---|
| $k_w$ | 0.617 | 0.946 | 0.946 | 0.617 |
| $N_p/N_s$ | 12/16 | 12/17 | 12/19 | 12/20 |
| $k_w$ | 0.866 | 0.933 | 0.933 | 0.866 |
| $N_p/N_s$ | 15/20 | 15/22 | 15/23 | 15/25 |
| $k_w$ | 0.866 | 0.952 | 0.952 | 0.866 |

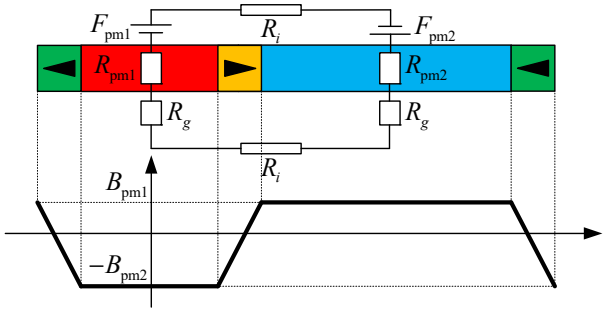


Fig. 3. Equivalent magnetic circuit model of Halbach PM array.

## III. ANALYTICAL MODELING AND CALCULATION

The proposed AFR-PMLM with Halbach PM array follows the principles of flux modulation theory and can be analytically calculated using the MMF-permeance model. To simplify the modeling process, certain assumptions are made: 1) neglecting the end effect and magnetic saturation, 2) neglecting the reluctance of the iron core, and 3) assuming infinite depth for the secondary slots.

### *A. MMF Produced by Halbach PM Array*

Fig. 3 depicts the equivalent magnetic circuit (EMC) model of the Halbach PM array with a slotless secondary. This EMC model allows for the calculation of the ideal air gap flux density distribution, considering the effect of the two secondary PMs in the Halbach PM array, which can be approximated as a trapezoidal waveform. Due to the unequal widths of the two main PMs in the Halbach PM array, the positive and negative amplitudes of the trapezoidal waveform are asymmetric and can

be calculated as follows:

$$\begin{cases} B_{\mathrm{pm1}} = 2(1-\beta)B_{\mathrm{r}} \big/ \left(1+g\mu_{\mathrm{r}}/h_{\mathrm{pm}}\right) \\ B_{\mathrm{pm2}} = 2\beta B_{\mathrm{r}} \big/ \left(1+g\mu_{\mathrm{r}}/h_{\mathrm{pm}}\right) \\ \beta = \left(w_{\mathrm{pml}}+w_{\mathrm{pmh}}\right)/l_{\mathrm{p}} \end{cases} \tag{3}$$

where $g$ is the length of air gap, $h_{\mathrm{pm}}$ is the PM height in the main magnetized direction, $\mu_{\mathrm{r}}$ and $B_{\mathrm{r}}$ are the relative permeability and remanence of the PMs, respectively, $w_{\mathrm{pml}}$ is the width of the main PM in the slot and $w_{\mathrm{pmh}}$ is the width of the secondary PM. Subsequently, the ideal air gap flux density without considering the secondary slot is defined as $B_{\mathrm{pm}}$ and can be calculated as:

$$B_{\mathrm{pm}}(x) = \sum_{i=1}^{\infty} \frac{2}{i\pi} B_{\mathrm{A}} \cos\left[ iN_{\mathrm{pm}} \frac{2\pi}{N_{\mathrm{p}} l_{\mathrm{p}}} x \right] \tag{4}$$

where the coefficients of Fourier Series $B_{\mathrm{A}}$ can be calculated by using the integral of the trapezoidal waveform in Fig. 3, $N_{\mathrm{pm}}$ represents the pole-pair number (PPN) of PMs. Based on this foundation, the MMF produced by Halbach PM array can be expressed as:

$$F_{\mathrm{pm}}(x) = g_{\mathrm{e}} B_{\mathrm{pm}} / \mu_0 = \sum_{i=1}^{\infty} \frac{2}{i\pi} \frac{B_{\mathrm{A}}}{\mu_0 / g_{\mathrm{e}}} \cos\left[ iN_{\mathrm{pm}} \frac{2\pi}{N_{\mathrm{p}} l_{\mathrm{p}}} x \right] \tag{5}$$

where $g_{\mathrm{e}}$ is the effective length of air gap, which includes an additional air gap $\delta_{\mathrm{p}}(x)$ caused by the Halbach PM array.

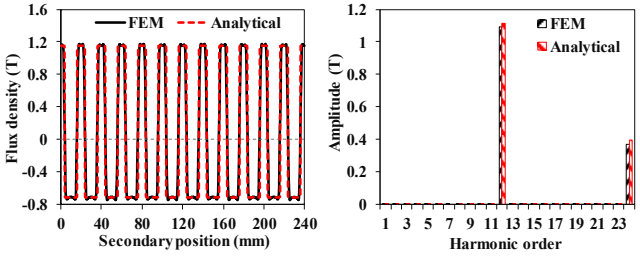


Fig. 4. Air gap flux density distribution with a slotless secondary.

Fig. 4 presents the air gap flux density distribution with a slotless secondary. The analytical results closely align with the corresponding FEM results, particularly concerning the peak amplitude. This validates the accuracy of the MMF modeling described by Eq. (3)-(5). Moreover, it is apparent that the proposed AFR-PMLM with Halbach PM array also exhibits asymmetry in the positive and negative parts of the MMF waveform due to the unequal widths of two main PMs. Then, the second-order harmonic MMF with the PPN of 24 emerges and can contribute to the thrust force generation.

### *B. Air Gap Flux Density Distribution*

Due to the large slotting structure in the secondary, additional air gap $\delta_{\mathrm{s}}(x)$ is utilized to represent the equivalent air gap in the secondary. The secondary permeance ($\Lambda_{\mathrm{s}}$) can be expressed as:

$$\begin{cases} \Lambda_{\mathrm{s}}(x,t) = \mu_0 / \left(g + \delta_{\mathrm{s}}(x,t)\right) \\ \delta_{\mathrm{s}}(x,t) = \begin{cases} 0, & x \notin \left[Vt + w_{\mathrm{st}}/2, Vt + \tau_{\mathrm{p}} - w_{\mathrm{st}}/2\right] \\ \lambda_1\lambda_2 / \left(\lambda_1 + \lambda_2\right), & x \in \left[Vt + w_{\mathrm{st}}/2, Vt + \tau_{\mathrm{p}} - w_{\mathrm{st}}/2\right] \end{cases} \\ \lambda_1 = \pi\left(x - w_{\mathrm{st}}/2\right)/2, \ \lambda_2 = \pi\left(\tau_{\mathrm{p}} - w_{\mathrm{st}}/2 - x\right)/2 \end{cases} \tag{6}$$

where the lengths of flux $\lambda_1$ and $\lambda_2$ are assumed to be quarter-circular. When multiplying the air gap flux density with slotless secondary in Eq. (4) by the secondary permeance in Eq. (6), the air gap flux density of the AFR-PMLM with a slotted secondary can be calculated as:

$$B_{\mathrm{g}}(x,t) = B_{\mathrm{pm}}(x)\Lambda_{\mathrm{rel}} = B_{\mathrm{pm}}(x)\frac{g\Lambda_{\mathrm{s}}}{\mu_0} \tag{7}$$

Then, the back-EMF of the machine can be calculated as:

$$E_{\mathrm{A}}(t) = -\frac{d\left(l_{\mathrm{s}}\int_0^{N_{\mathrm{p}}l_{\mathrm{p}}} B_g(x,t) N_{\mathrm{A}}(x)\,dx\right)}{dt} \tag{8}$$

where $l_{\mathrm{s}}$ is the stack length and $N_{\mathrm{A}}(x)$ is the winding function.

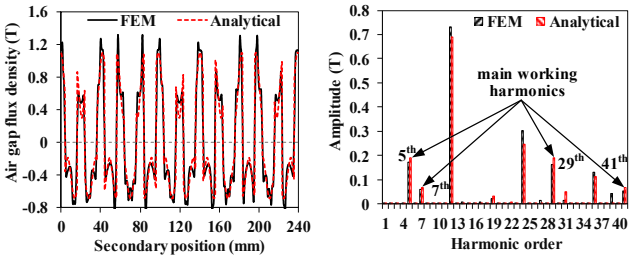


Fig. 5. Air gap flux density distribution with a slotted secondary.

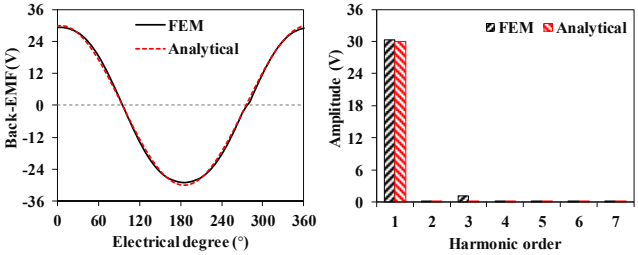


Fig. 6. Waveform of back-EMF and harmonics.

TABLE II
HARMONIC AMPLITUDES AND FORCE CONTRIBUTIONS OF AFR-PMLM

| MMF Order | Items | | Value |
|---|---|---|---|
| 1st | $\lvert N_{\mathrm{pm}} \pm N_{\mathrm{s}} \rvert$ 5th, 29th | Amplitude (T) | 0.188 |
| | | Force (N) | 211.5 |
| 2nd | $\lvert 2N_{\mathrm{pm}} \pm N_{\mathrm{s}} \rvert$ 7th, 41st | Amplitude (T) | 0.067 |
| | | Force (N) | 53.8 |
| 3rd | $\lvert 3N_{\mathrm{pm}} \pm N_{\mathrm{s}} \rvert$ 19th, 53rd | Amplitude (T) | 0.031 |
| | | Force (N) | 10.6 |

Fig. 5 illustrates the air gap flux density distribution and harmonics of the AFR-PMLM with a slotted secondary. The predicted analytical results are in good agreement with the FEM results. It is observed that harmonics with a PPN of 12 and 24 remain stationary, whereas harmonics with a PPN of 5, 7, 29, and 41 are moving and have the potential to induce back-EMF in the winding. Fig. 6 depicts the analytical results of back-EMF and its harmonics of the AFR-PMLM based on Eq. (8). The analytical results align well with the FEM predicted results, with a difference in fundamental amplitude within 1.1%. This comparison validates the accuracy of the analytical calculation for the proposed AFR-PMLM with Halbach PM array. Moreover, based on the fundamental waveform of the back-EMF obtained from Eq. (8) and by injecting a sinusoidal current, the electromagnetic force can be calculated, as shown in Table II. It can be observed that the fundamental MMF contributes nearly 76.6% of the electromagnetic force, while the second-order MMF contributes approximately 19.6%. The additional second-order MMF effectively generates more thrust force while maintaining the same PM volume.

## IV. ELECTROMAGNETIC PERFORMANCE ANALYSIS

To maximize the thrust force density, a global optimization combined with finite element method is conducted for the proposed AFR-PMLM equipped with a Halbach PM array. The optimization employs a genetic algorithm (GA), utilizing

natural selection to identify the optimal design. Specific machine specifications are fixed for effective optimization. These include the primary slot pitch set at 20 mm, machine height at 45 mm, stack length at 50 mm, and air gap at 0.8 mm. Additionally, N48UH and 50D470 are chosen as the materials for the PMs and primary, respectively.

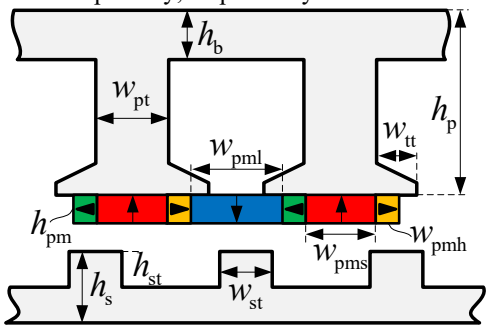


Fig. 7. Geometric parameters of AFR-PMLM with Halbach PM array.

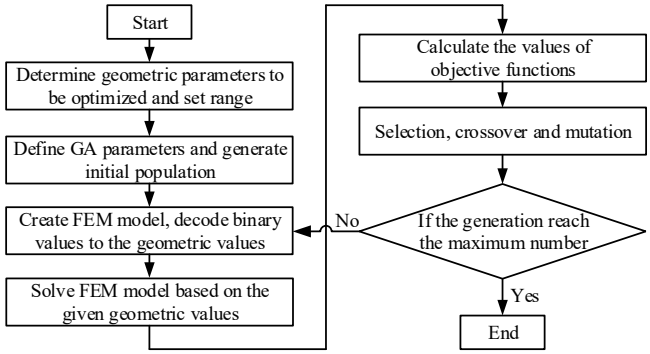


Fig. 8. FEM-coupled global optimization flow chart.

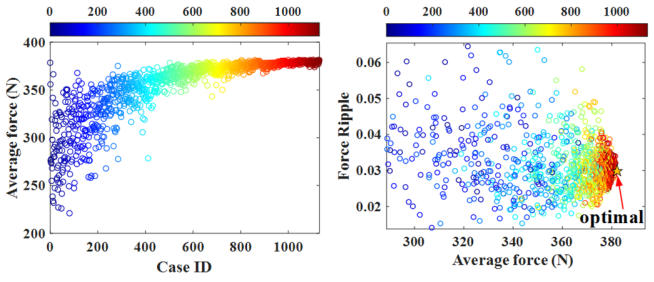


Fig. 9. Global optimization procedure and optimal selection of AFR-PMLM with Halbach PM array. (a) Variation of average force with case. (b) Iterative process and optimal selection.

Fig. 8 presents the FEM-coupled global optimization flow chart for the proposed AFR-PMLM with a Halbach PM array. The proposed GA can find the optimal design through natural selection, involving three operators: selection, crossover, and mutation. Geometric parameters shown in Fig. 7 are encoded, with each case represented by a chromosome during the optimization process. The number of populations and generations in GA is selected as 50 each, and the crossover and mutator factors are 0.9 and 0.1, respectively. Additionally, there are two optimization objectives: 1) maximizing the average force with a weight coefficient of 0.8, and 2) minimizing the force ripple with a weight coefficient of 0.2. Fig. 9 illustrates the global optimization procedure and the optimal selection of the AFR-PMLM with Halbach PM array. The color bar that ranging from blue to red, represents the iteration of cases. It can be observed that the average force gradually increases and converges as the GA evolves. After evaluating thousands of cases, the solutions converge from the initial blue circles towards an optimal region represented by the red circles. This convergence allows for the selection of the optimal design, characterized by relatively high thrust force and low force ripple. Finally, the optimal geometric parameters and specifications of the proposed AFR-PMLM with Halbach PM array are listed in Table III.

TABLE III
DESIGN PARAMETERS OF 12S17P AFR-PMLM WITH HALBACH PM ARRAY

| Symbol | Parameters | Units | Value |
|---|---|---|---|
| Globally optimized geometric parameters | | | |
| $\tau$ | Secondary pole pitch | mm | 14.12 |
| $k_{sr}$ | Split ratio | / | 0.25 |
| $w_{pt}$ | Primary tooth width | mm | 7.5 |
| $w_{pms}$ | Main PM width - tooth | mm | 6.0 |
| $w_{pml}$ | Main PM width - slot | mm | 10.6 |
| $w_{pmh}$ | Secondary PM width | mm | 1.7 |
| $h_{pm}$ | PM height | mm | 1.7 |
| $w_{tt}$ | Tooth tip width | mm | 4.2 |
| $h_p$ | Primary height | mm | 32.0 |
| $h_{bi}$ | Back iron height | mm | 6.0 |
| $h_{st}$ | Secondary pole height | mm | 5.6 |
| $w_{st}$ | Secondary pole width | mm | 4.6 |
| $h_s$ | Secondary height | mm | 10.5 |
| Rated data | | | |
| $k_f$ | Coil filling factor | / | 0.55 |
| $P_{cop}$ | Rated copper dissipation | W | 200 |
| $N$ | Number of turns | / | 115 |
| $I$ | Rated phase current | A | 6.2 |

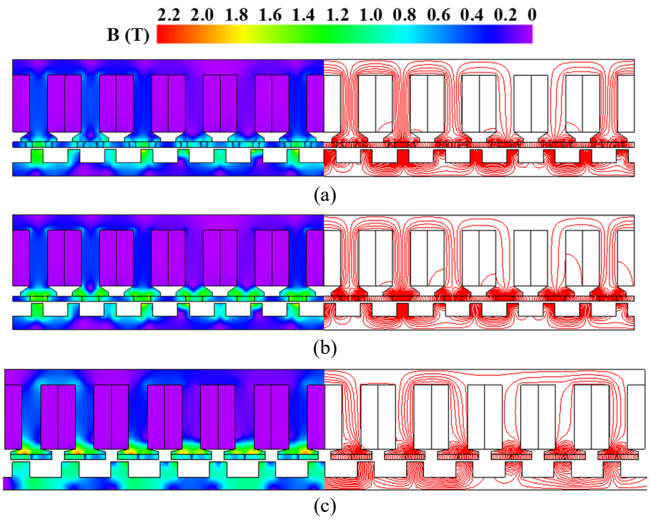


Fig. 10. Open-circuit magnetic field distribution of AFR-PMLM. (a) Halbach PM array. (b) Conventional asymmetric PM excitation. (c) Conventional FR-PMLM with symmetric PM excitation.

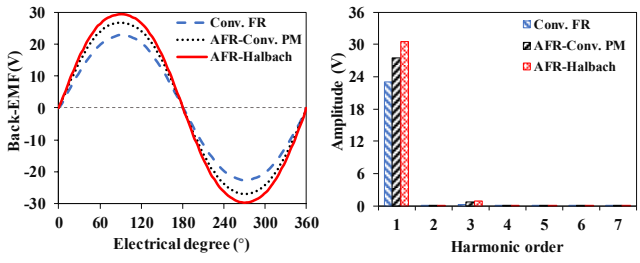


Fig. 11. Comparison of open-circuit phase back-EMFs in AFR-PMLM at a velocity of 1.0 m/s. (a) Waveforms. (b) Harmonics.

### *A. Open-Circuit Performance*

Fig. 10 presents the open-circuit magnetic field distribution

of the AFR-PMLM. Notably, the majority of the leakage flux is concentrated near the PM excitation region, while saturation in the primary tooth and back iron regions is minimal. Furthermore, due to the opposite magnetization of the two secondary PMs in the Halbach PM array relative to the leakage flux loop, significant reduction in leakage flux is achieved and some of it is redirected into the main flux. Consequently, the implementation of the Halbach PM array effectively alleviates magnetic saturation. Fig. 11 comparatively studies the open-circuit phase back-EMFs between two types of AFR-PMLM and conventional FR-PMLM. It should be noted that both the AFR-PMLM with conventional asymmetric PM excitation and the conventional FR-PMLM have undergone global optimization, similar to the proposed machine. The results indicate that the AFR-PMLM with conventional asymmetric PM excitation yields a 20% higher amplitude than the conventional FR-PMLM with symmetric PM excitation. Moreover, the AFR-PMLM with Halbach PM array exhibits a further increase in amplitude by over 10.8% compared to the AFR-PMLM with conventional asymmetric PM excitation. Thus, the Halbach PM array proves effective in enhancing the back-EMF amplitude.

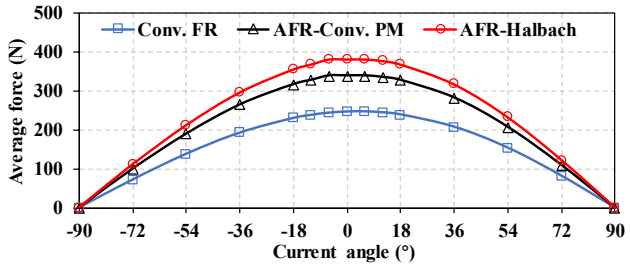


Fig. 12. Variation of average force across various current angles.

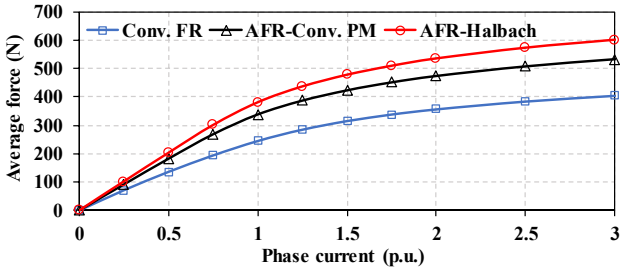


Fig. 13. Variation of average force across various phase currents.

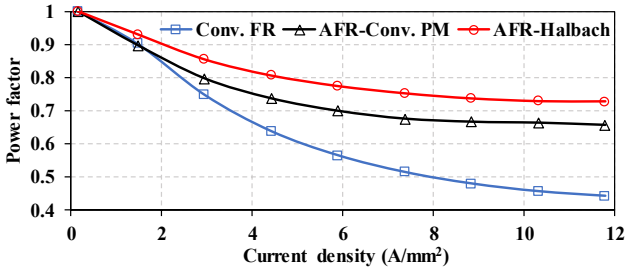


Fig. 14. Variation of power factor with different current densities.

### B. On-Load Performance

Fig. 12 illustrates the variation of average force across various current angles. It is evident that all three types of FR-PMLM achieve maximum force when the current angle approaches zero. This observation implies that there is minimal reluctance effect, and a simplified $i_d = 0$ control strategy can be effectively employed for these machines. Fig. 13 investigates the variation of average force across various phase currents. As observed, the AFR-PMLM with Halbach PM array can provide 12.8% and 55.4% higher average force than that in AFR-PMLM with conventional asymmetric PM excitation and conventional FR-PMLM, respectively. Fig. 14 depicts a comparison of the power factor among three types of machines. The results suggest that the Halbach PM array can significantly improve the power factor by reducing the leakage flux. At a current density of 6 A/mm$^2$, the power factor can be increased by over 10.7% to exceed 0.77. Furthermore, it is clear that employing asymmetric PM excitation can significantly boost the power factor by 36.8% compared to conventional FR-PMLM with symmetric PM excitation.

Fig. 15 presents the thermal performance of the machine under rated copper dissipation. Since the primary exhibits a back-and-forth motion, it can be considered as having forced air cooling, and the working duty is not continuous. After 120 minutes of operation, the temperature tends to stabilize from the initial 20°C, with the maximum temperature at the end winding reaching about 93.9°C. Therefore, this machine can operate safely at temperatures up to 100°C without posing a risk of irreversible demagnetization to the PMs. However, if it operates in an overloaded state for an extended period, effective thermal management such as water cooling is required.

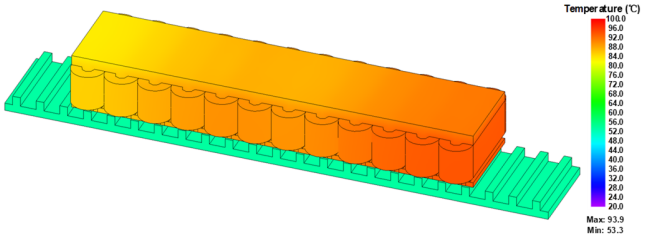


Fig. 15. Temperature distribution under rated copper dissipation.

TABLE IV
PERFORMANCE COMPARISON WITH CONVENTIONAL PMLM

| Performance | Conventional PMLM | AFR-PMLM with Halbach PM Array |
|---|---|---|
| Average force (N) | 528.3 | 381.0 |
| Detent force (N) | 56.4 | 13.1 |
| Force ripple (%) | 16.3 | 3.0 |
| PM Vol. (mL) (@10 m) | 1660.0 | 20.4 |
| PM Vol. (mL) (@0.24 m) | 39.8 | 20.4 |
| Force density (N/L) | 978.3 | 705.6 |

### C. Performance Comparison

To evaluate the electromagnetic performance, particularly thrust force density and PM consumption under long-distance applications, Table IV provides a fair comparison with a conventional PMLM of identical external dimensions and a copper loss of 200 W. This conventional PMLM has also undergone global optimization. The key difference between the conventional PMLM and the proposed AFR-PMLM lies in the placement of PMs, as the conventional PMLM requires PMs to be mounted along the entire length of the secondary. The results show that the proposed AFR-PMLM with Halbach PM array can provide nearly 72.1% of the thrust force density while consuming only 1/81 of the PMs over a 10-meter distance. Even at a unit distance of 0.24 meters, the proposed AFR-PMLM consumes only half the PMs.

## V. Prototype and Experimental Validation

To assess the electromagnetic performance of the proposed AFR-PMLM with Halbach PM array, this section encompasses the fabrication and experimental validation of a 12s17p AFR-PMLM prototype, as shown in Fig. 16. The geometric parameters of the prototype align with those listed in Table III. The primary is mounted on a mover guided by two linear guides, while the secondary is positioned on the stator between two linear guides. Additionally, the test bench comprises two components: the prototype platform and an air-core PMLM. These two components are interconnected via a force meter capable of recording force.

During the testing of the open-circuit phase back-EMFs of the prototype, the air-core PMLM is driven to maintain a steady-state velocity. In Fig. 17(a), the test results of three-phase open-circuit back-EMFs at a velocity of 0.3 m/s are plotted. The outcomes closely approximate those obtained through FEM, with discrepancies among the three phases determined to be 5.5%, 4.2%, and 5.8%, respectively. Additionally, Fig. 17(b) presents the test results of thrust force with various phase currents. The data reveals a consistent alignment between the variations in tested thrust force results and the FEM predictions, further confirming that the prototype adheres to the design criteria.


Fig. 16. The prototype of 12s17p AFR-PMLM and test bench for experiment.

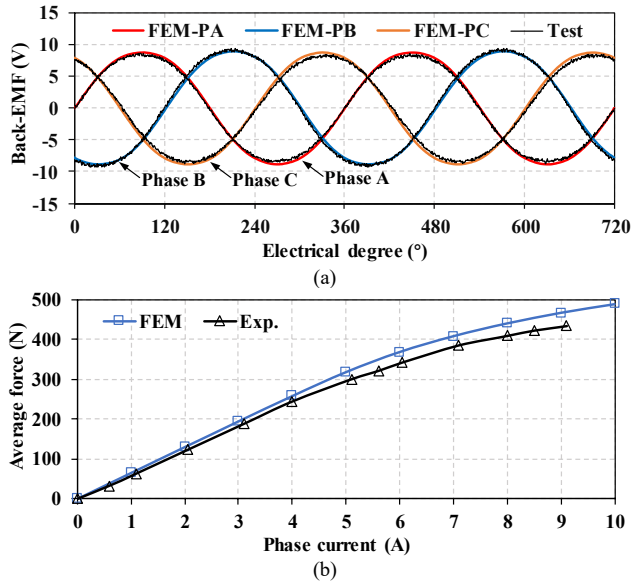


Fig. 17. Test results of the prototype. (a) Open-circuit phase back-EMF at a velocity of 0.3 m/s. (b) On-load thrust force with different phase currents.

## VI. Conclusion

This paper introduces a novel type of AFR-PMLM with Halbach PM array designed specifically for long distance applications. The thrust force generation mechanism under multiple MMFs is analytically calculated based on flux modulation theory. The electromagnetic performances are thoroughly illustrated and comprehensively studied. Some conclusions can be drawn as follows:

1) By utilizing asymmetric Halbach PM array, the second-order harmonic MMF emerges and constitutes nearly 34% of the fundamental amplitude, rendering it a valuable resource for enhancing thrust force density. Therefore, the construction and utilization of multiple MMFs represent an effective approach for increasing thrust force density.

2) With the help of the Halbach PM array, some magnetic flux can be redirected from the leakage flux into the main flux. This results in a power factor exceeding 0.77 under a current density of 6 A/mm$^2$, representing a significant improvement of 36.8% compared to conventional FR-PMLM with symmetric PM excitation.

3) The proposed AFR-PMLM with Halbach PM array demonstrates the capability to provide 12.8% and 55.4% higher average force than that in AFR-PMLM with conventional asymmetric PM excitation and conventional FR-PMLM, respectively. Compared with conventional PMLM, it can provide nearly 72.1% of the thrust force density while consuming only 1/81 of the PMs over a 10-meter distance.

## Acknowledgment

This work was supported in part by the National Natural Science Foundation of China under Grant 52107060, and in part by the Zhejiang Provincial Natural Science Foundation of China under Grant LQ22E070003.

## References

[1] I. Boldea, L. N. Tutelea, W. Xu and M. Pucci, "Linear Electric Machines, Drives, and MAGLEVs: An Overview," IEEE Trans. Ind. Electron., vol. 65, no. 9, pp. 7504-7515, Sep. 2018.

[2] C. Guo, Z. Zuo, H. Feng, et al, "Review of recent advances of free-piston internal combustion engine linear generator," Appl. Energy, vol. 269, 115084, Jul. 2020.

[3] Y. Shen, Q. Lu, "Overview of Permanent Magnet Linear Machines with Primary Excitation," Trans. China Electrotechnical Society, vol. 36, no.11, pp. 2325-2343, Jun. 2021.

[4] X. Huang, J. Liang, B. Zhou, C. Zhang, L. Li and D. Gerada, "Suppressing the Thrust Ripple of the Consequent-Pole Permanent Magnet Linear Synchronous Motor by Two-Step Design," IEEE Access, vol. 6, pp. 32935-32944, 2018.

[5] X. Huang, Z. Qian, Q. Tan, J. Li and B. Zhou, "Suppressing the Thrust Ripple of the Permanent Magnet Linear Synchronous Motors with Different Pole Structures by Setting the Modular Primary Structures Differently," IEEE Trans. Energy Convers., vol. 33, no. 4, pp. 1815-1824, Dec. 2018.

[6] Y. Shen, Q. Lu, H. Li, J. Cai, X. Huang and Y. Fang, "Analysis of a Novel Double-Sided Yokeless Multitooth Linear Switched-Flux PM Motor," IEEE Trans. Ind. Electron., vol. 65, no. 2, pp. 1837-1845, Feb. 2018.

[7] L. Wu, L. Zhang, J. Zhu, Q. Lu and Y. Fang, "Comparative Study of Novel Doubly-Fed Linear Switched Flux Permanent Magnet Machines with Different Primary Structures," IEEE Access, vol. 8, pp. 69401-69412, 2020.

[8] C. -T. Liu, C. -C. Hwang, P. -L. Li, S. -S. Hung and P. Wendling, "Design Optimization of a Double-Sided Hybrid Excited Linear Flux Switching PM Motor with Low Force Ripple," IEEE Trans. Magn., vol. 50, no. 11, pp. 1-4, Nov. 2014.

[9] Y. Shen and Q. Lu, "Design and Analysis of Hybrid-Excited Flux Modulated Linear Machines with Zero-Sequence Current Excitation," IEEE J. Emerg. Sel. Topics Power Electron., vol. 10, no. 2, pp. 1834-1846, Apr. 2022.

[10] N. J. Baker, M. A. H. Raihan, A. A. Almoraya, J. W. Burchell and M. A. Mueller, "Evaluating Alternative Linear Vernier Hybrid Machine Topologies for Integration into Wave Energy Converters," IEEE Trans. Energy Convers., vol. 33, no. 4, pp. 2007-2017, Dec. 2018.

[11] A. A. Almoraya, N. J. Baker, K. J. Smith and M. A. H. Raihan, "Design and Analysis of a Flux-Concentrated Linear Vernier Hybrid Machine with Consequent Poles," IEEE Trans. Ind. Appl., vol. 55, no. 5, pp. 4595-4604, Sept.-Oct. 2019.

[12] W. Zhao, J. Zheng, J. Wang, G. Liu, J. Zhao and Z. Fang, "Design and Analysis of a Linear Permanent- Magnet Vernier Machine with Improved Force Density," IEEE Trans. Ind. Electron., vol. 63, no. 4, pp. 2072-2082, Apr. 2016.

[13] Y. Shen, Z. Li, Z. Zeng, Q. Lu and C. H. T. Lee, "Quantitative Analysis of Asymmetric Flux Reversal Permanent Magnet Linear Machine for Long Excursion Application," *IEEE Trans. Ind. Electron.*, doi: 10.1109/TIE.2023.3344854.